Nuclear Science and Techniques (2026) 37:9
https://doi.org/10.1007/s41365-025-01815-z

Neutron-gamma density measurement method using the mass attenuation coefficient function

Jun-Yan Chen[1] · **Qiong Zhang**[1]

Received: 5 November 2024 / Revised: 23 April 2025 / Accepted: 9 June 2025 / Published online: 6 December 2025

Abstract

Although traditional gamma-gamma density (GGD) logging technology is widely utilized, its potential environmental risks have prompted the development of more environmentally friendly neutron-gamma density (NGD) logging technology. However, NGD measurements are influenced by both neutron and gamma radiations. In the logging environment, variations in the formation composition indicate different elemental compositions, which affect the neutron-gamma reaction cross-sections and gamma generation. Compared to traditional gamma sources such as Cs-137, these changes significantly affect the generation and transport of neutron-induced inelastic gamma rays and hinder accurate measurements. To address this, a novel method is proposed that incorporates the mass attenuation coefficient function to account for the effects of various lithologies and pore contents on gamma-ray attenuation, thereby achieving more accurate density measurements by clarifying the transport processes of inelastic gamma rays with varying energies and spatial distributions in varied logging environments. The proposed method avoids the complex correction of neutron transport and is verified through Monte Carlo simulations for its applicability across various lithologies and pore contents, demonstrating absolute density errors that are less than 0.02 g/cm^3 in clean formations and indicating good accuracy. This study clarifies the NGD mechanism and provides theoretical guidance for the application of NGD logging methods. Further studies will be conducted on extreme environmental conditions and tool calibration.

Keywords Neutron-gamma density · Mass attenuation coefficient · Monte Carlo simulation

Nomenclature

GGD	Gamma-gamma density
NGD	Neutron-gamma density
ϕ_n	Fast neutron distribution
Q	Number of neutrons emitted per second
D_n	Neutron diffusion coefficient
L_n	Fast neutron deceleration length
r	Distance between the source and detector
i	Average number of inelastic gamma rays after the neutron enters the formation
Σ_{in}	Inelastic scattering cross-section
Φ_{in}	Inelastic gamma-ray distribution
L_1	Distance of the near-gamma detector
L_2	Distance of the far-gamma detector
ρ	Formation density
μ_m	Total mass attenuation coefficient
I_H	Hydrogen index
E_0	Initial energy of fast neutrons
μ_{co}	Mass attenuation coefficient for the Compton effect
μ_{pa}	Mass attenuation coefficient for pair production
N_A	Avogadro's constant
A	Atomic weight
Z	Atomic number
l	Formation lithology
p	Pore content
r_0	Classical electron radius
E_γ	Gamma-ray energy
DT	True density of the simulated formation
DC	Calculated density
m_e	Electron rest mass
c	Speed of light in vacuum

This work was supported by the National Natural Science Foundation of China (U23B20151 and 52171253).

✉ Qiong Zhang
zhanqio@uestc.edu.cn

[1] University of Electronic Science and Technology of China, Chengdu 611731, China

Sigma	Formation macroscopic capture cross-section
FN1	Near-fast neutron count
FN2	Far-fast neutron count
ETN1	Near-epithermal neutron count
ETN2	Far-epithermal neutron count
CAP1	Near-captured gamma count
CAP2	Far-captured gamma count
IN1	Near-inelastic gamma count
IN2	Far-inelastic gamma count
RFN	Ratio of the near-to-far fast neutron counts
RETN	Ratio of the near-to-far epithermal neutron counts
RCAP	Ratio of the near-to-far capture gamma counts
RIN	Ratio of the near-to-far inelastic gamma counts

1 Introduction

In the field of petroleum exploration, traditional gamma-gamma density (GGD) logging technology has played a crucial role for many years [1–5]. However, the growing awareness of environmental protection has made the risks of pollution and operational safety associated with GGD technology increasingly apparent, posing challenges for its further development. In this context, neutron-gamma density (NGD) logging technology has attracted attention owing to its advantages of environmental protection and controllability [6–10]. GGD relies on the transport of monoenergetic gamma rays from the source to the detectors, whereas NGD is based on the transport of neutron-induced gamma rays whose energy exhibits uncertainty. In NGD, the gamma rays detected by the detector are influenced by neutron transport from the neutron source to the point of the gamma-ray-producing neutron interaction in the formation and by the subsequent transport of the gamma rays from their source to the gamma-ray detector. The influence of thermal neutron effects was eliminated by conducting density measurements using inelastic gamma rays produced by high-energy neutrons [11, 12]. The emitted neutrons undergo inelastic scattering reactions with the isotopes of crucial elements in the medium within a few microseconds, producing inelastic gamma rays. These gamma rays are less influenced by neutron transport, enabling them to reflect the formation characteristics more accurately and increasing their suitability for density measurements. However, evaluating inelastic gamma rays can be difficult because they depend on both neutron and gamma physics and simultaneously undergo multiple physical processes. Hence, entanglement between the neutron and gamma transport increases the complexity of the measurement and its sensitivity to the environment. The generation and attenuation of inelastic gamma rays are directly influenced by environmental factors such as lithology, porosity, and fluid properties. Understanding both the neutron and gamma physics pertaining to changing environments is critical for developing an accurate method for NGD technology [13–15].

NGD technology has been actively developed over the past few decades. For instance, Odom et al. used inelastic gamma rays for density measurements, which was based on the neutron-gamma coupled field [16, 17]. However, this method was affected by neutron transport, and neutron transport corrections must be considered in subsequent studies. Jacobson et al. developed a correction technique that employed the captured gamma count ratio to obtain a compensated inelastic gamma ratio, thereby achieving density measurements [18]. Zhang et al. developed a density method that used the inelastic gamma count ratio and fast neutron count to avoid neutron correction [19]. Luycx et al. approximated the initial inelastic gamma flux by using fast neutron counts for density measurements [20]. Wang et al. created a correction model utilizing epithermal neutrons and divided the inelastic gamma ray energy spectrum into high- and low-energy windows to reduce the influence of pair production [21]. Additionally, Zhang et al. introduced an adaptive method for obtaining inelastic gamma spectra during environmental changes and an integrated capture correction for density measurements [22]. While these studies have made progress, researchers have primarily focused on analyzing the neutron transport process and less on the dynamic changes during gamma attenuation. Inelastic gamma rays generated by neutron-induced reactions exist in formations with a non-monoenergetic distribution, whereas chemical sources such as Cs-137 generate monoenergetic gamma rays in a homogeneous manner. Furthermore, typical neutron-induced gamma rays can reach energies of up to 8 MeV [23]. Pair production must be considered because of its vital role in the neutron-induced gamma transport process. These factors increase the complexity of gamma attenuation. Previous NGD and GGD measurements provided possibilities for density measurements. However, most previous NGD methods considered the mass attenuation coefficient as a constant, which limited the accuracy because it was closely related to the formation composition. In this study, we introduce the mass attenuation coefficient as a function related to the formation lithologies and pore contents to accurately depict the intricate interaction mechanisms between radiation and formation, which is essential for obtaining an accurate formation density. Additionally, this provides a new approach to complement previous methods.

The remainder of this paper is organized as follows: Sect. 2 introduces the method and presents the development process. In addition, a pulsed neutron density tool that was subsequently employed for concept verification is described. Section 3 presents the results for the different simulated scenarios and demonstrates the effectiveness of the method. Finally, conclusions are presented in Sect. 4.

2 Method

The development of the method is shown in Fig. 1: Box1 reviews the coupled field theory of NGD measurements, which is the foundation for the proposed method because it depicts the distribution of inelastic gamma rays. Box2 is the key to the method. A function for the mass attenuation coefficient is developed, which is then used to derive the density. Certain key parameters, such as the hydrogen index that cannot be directly expressed in this mathematical form, are obtained through tool measurements. Box3 presents an analysis of the physical parameters using a real NGD tool during the development stage. Extensive Monte Carlo simulations are conducted to establish a quantitative relationship between the detector responses and physical parameters of the formation, which is utilized to obtain these key parameters. Finally, the density is calculated.

2.1 Coupled field theory of NGD measurement

NGD logging technology relies on inelastic gamma rays to measure the formation density [24–29]. The distribution of inelastic gamma rays involves two interconnected links between neutrons and gamma transport [30–32], as described below.

The pulsed neutron source emitted 14 MeV fast neutrons. According to the neutron diffusion theory, the distribution of fast neutrons in a spherical model can be described as follows:

$$\Phi_{\mathrm{n}} = \frac{Q}{4\pi D_{\mathrm{n}} r} \exp\left(-\frac{r}{L_{\mathrm{n}}}\right), \tag{1}$$

where Q, D_{n}, L_{n}, and r denote the number of neutrons emitted by the neutron source per second, neutron diffusion coefficient, fast neutron deceleration length, and distance between the pulsed neutron source and neutron detector, respectively. The inelastic gamma rays recorded by a detector with a radius R can be described by the following Eq. [21]:

$$\Phi_{\mathrm{in}}(R) = \frac{i\Sigma_{\mathrm{in}} Q \int_0^{\infty} \exp(-\frac{r}{L_{\mathrm{n}}} \exp(-\rho\mu_{\mathrm{m}}|r-R|))\mathrm{d}r}{4\pi D_{\mathrm{n}} R}, \tag{2}$$

where i, Σ_{in}, ρ, and μ_{m} denote the average number of inelastic gamma rays after the neutron enters the formation, inelastic scattering cross-section, formation density, and total mass attenuation coefficient, respectively. The inelastic gamma

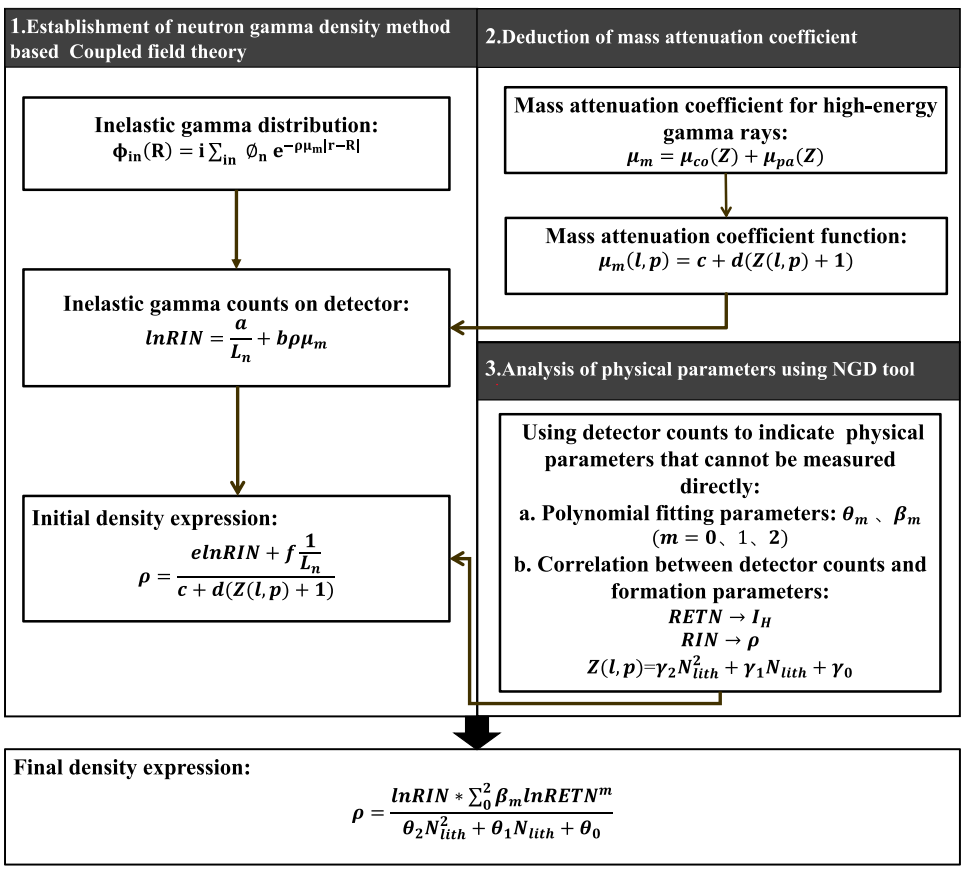

Fig. 1 (Color online) Overview of the proposed method

rays within a distance from the source R are recorded [33], and Eq. (2) can be written as

$$\Phi_{\text{in}}(R) = \frac{i\Sigma_{\text{in}}Q}{4\pi D_{\text{n}}R}\frac{\exp\left(-\frac{R}{L_{\text{n}}}\right) - \exp(-\rho\mu_{\text{m}}R)}{\rho\mu_{\text{m}} - \frac{1}{L_{\text{n}}}}. \tag{3}$$

According to the Lagrange interpolation method, Equation (3) can be simplified as follows:

$$\Phi_{\text{in}}(R) = \frac{i\Sigma_{\text{in}}Q}{4\pi D_{\text{n}}}\exp(-R\xi). \tag{4}$$

Here, ξ belongs to $\left(\rho\mu_{\text{m}}, \frac{1}{L_{\text{n}}}\right)$ and can be expressed as: $\xi = \frac{1}{L_{\text{n}}} - \alpha\left(\frac{1}{L_{\text{n}}} - \rho\mu_{\text{m}}\right), \alpha \in (0, 1)$.

Assuming that the source distances of the near- and far-gamma detectors are $L1$ and $L2$ ($L1 < L2$), respectively, the following equations are obtained:

$$\begin{cases} \Phi_{\text{in}}(L_1) = \frac{i\Sigma_{\text{in}}Q}{4\pi D_{\text{n}}}\exp(-L_1\xi_1) \\ \Phi_{\text{in}}(L_2) = \frac{i\Sigma_{\text{in}}Q}{4\pi D_{\text{n}}}\exp(-L_2\xi_2) \end{cases} \tag{5}$$

where

$$\begin{cases} \xi_1 = \frac{1}{L_{\text{n}}} - \alpha_1\left(\frac{1}{L_{\text{n}}} - \rho\mu_{\text{m}}\right), \alpha_1 \in (0, 1) \\ \xi_2 = \frac{1}{L_{\text{n}}} - \alpha_2\left(\frac{1}{L_{\text{n}}} - \rho\mu_{\text{m}}\right), \alpha_2 \in (0, 1) \end{cases} \tag{6}$$

The logarithm of the ratio of the near- and far-inelastic gamma counts is given by:

$$\begin{aligned} \ln(\text{RIN}) &= \ln\left(\frac{\Phi_{\text{in}}(L_1)}{\Phi_{\text{in}}(L_2)}\right) \\ &= \frac{L_1\alpha_1 - L_2\alpha_2 + L_2 - L_1}{L_{\text{n}}} + (L_2\alpha_2 - L_1\alpha_1)\rho\mu_{\text{m}}. \end{aligned} \tag{7}$$

If $a = L_1\alpha_1 - L_2\alpha_2 + L_2 - L_1$, $b = L_2\alpha_2 - L_1\alpha_1$, Equation (7) can be reorganized:

$$\ln(\text{RIN}) = \frac{a}{L_{\text{n}}} + b\rho\mu_{\text{m}}. \tag{8}$$

Equation (8) shows that the response of the gamma-ray detector is related to the L_{n}, ρ, μ_{m}, and the values of a and b. In typical formations, the fast neutron deceleration length (L_{n}) is characterized by the formation density ρ, hydrogen index I_{H}, and initial energy of the fast neutron E_0 [34]. Thus,

$$L_{\text{n}} = k\sqrt{\frac{1}{I_{\text{H}} + c}}\sqrt{\frac{1}{\rho}}\sqrt{\ln(E_0)}. \tag{9}$$

The key parameter in Eq. (8) is the mass attenuation coefficient μ_{m}, which directly reflects the attenuation of gamma rays in the formation and is analyzed in the following section .

2.2 Development of the NGD method

The attenuation of gamma rays in formations is closely linked to the formation density and mass attenuation coefficient. The attenuation is primarily influenced by various physical processes, including the photoelectric effect, Compton effect, and pair production. The Compton effect and pair production are the primary factors that affect the attenuation of high-energy gamma rays. Thus, the total attenuation coefficient μ_{m} can be expressed as:

$$\mu_{\text{m}} = \mu_{\text{co}} + \mu_{\text{pa}}, \tag{10}$$

where μ_{co} and μ_{pa} denote the mass attenuation coefficients for the Compton effect and pair production, respectively.

According to the principles of the Compton effect and pair production [35, 36], their mass attenuation coefficients can be expressed as:

$$\begin{aligned} \mu_{\text{co}} =& 2\pi(r_0)^2\left\{\frac{1+\eta}{\eta^2}\left[\frac{2(1+\eta)}{1+2\eta} - \frac{1}{\eta}\ln(1+2\eta)\right]\right. \\ &\left. + \frac{1}{2\eta}\ln(1+2\eta) - \frac{1+3\eta}{(1+2\eta)^2}\right\}N_{\text{A}}\frac{Z}{A}, \end{aligned} \tag{11}$$

$$\mu_{\text{pa}} = \frac{(r_0)^2N_{\text{A}}}{137}\left(\frac{28}{9}\ln(2\eta) - \frac{218}{27}\right)(Z+1)\frac{Z}{A}, \tag{12}$$

where N_{A} is the Avogadro constant; r_0 is the classical electron radius ($r_0 = 2.818 \times 10^{-13}$ cm); $\eta = \frac{E_\gamma}{m_{\text{e}}c^2}$; E_γ is the gamma-ray energy; m_{e} is the electron rest mass ($m_{\text{e}} = 9.110 \times 10^{-31}$ kg); c is the speed of light in vacuum ($c = 2.998 \times 10^8$ m/s); Z is the atomic number; and A is the atomic weight. The total mass attenuation coefficient can be rewritten as:

$$\begin{aligned} \mu_{\text{m}} =& \pi(r_0)^2\left\{\frac{1+\eta}{\eta^2}\left[\frac{2(1+\eta)}{1+2\eta} - \frac{1}{\eta}\ln(1+2\eta)\right]\right. \\ &\left. + \frac{1}{2\eta}\ln(1+2\eta) - \frac{1+3\eta}{(1+2\eta)^2}\right\}N_{\text{A}} \\ &+ \frac{(r_0)^2N_{\text{A}}}{274}\left(\frac{28}{9}\ln(2\eta) - \frac{218}{27}\right)(Z+1). \end{aligned} \tag{13}$$

Equation 13 shows the impact of the gamma ray energy E_γ and formation atomic number Z on the mass attenuation coefficient μ_{m}, highlighting the response sensitivity among these variables. Unlike previous studies, where the mass attenuation coefficient was typically assumed to be constant, the present study emphasizes its variability. However, changes in the mass attenuation coefficient within the average energy range of inelastic gamma rays in formations are

sufficiently small to ignore the effect of gamma energy [37]. Instead, its close correlation with the composition of the formation is emphasized, particularly the effects of lithology and pore content on the macroscopic atomic number (Z). This aspect is further confirmed by Fig. 2, which shows the differences in the macroscopic atomic numbers of the formation when the lithology and porosity content change. These changes in the lithology and pore content indicate variations in the constituent elements of the formation, which directly affect the formation macroscopic atomic number (Z) and alters the total mass attenuation coefficient. This affects gamma ray attenuation, thereby complicating gamma ray transport. Therefore, the mass attenuation coefficient is treated as a function of the formation lithology (l) and pore content (p). Accurate density measurements can be achieved by describing the influence of the different formation components on the gamma transport process.

According to the preceding analysis, treating the mass attenuation coefficient as a function of the environmental parameters is expected to better depict the gamma formation reaction sensitivity and improve the accuracy of NGD calculations. Thus,

$$\mu_{\mathrm{m}}(l,p) = c + d(Z(l,p)+1), \tag{14}$$

$$\begin{aligned} \mathrm{c} =& \pi (r_0)^2 N_{\mathrm{A}} \left\{ \frac{1+\eta}{\eta^2} \left[\frac{2(1+\eta)}{1+2\eta} - \frac{1}{\eta} \ln(1+2\eta) \right] \right. \\ & \left. + \frac{1}{2\eta} \ln(1+2\eta) - \frac{1+3\eta}{(1+2\eta)^2} \right\}, \end{aligned} \tag{15}$$

$$d = \frac{(r_0)^2 N_{\mathrm{A}}}{274} \left(\frac{28}{9} \ln(2\eta) - \frac{218}{27} \right), \tag{16}$$

where c and d are constants.

After substituting the mass attenuation coefficient μ_{m} from Eq. 14 into Eq. 8, the equation can be rewritten as:

$$\rho = \frac{e \ln(\mathrm{RIN}) + f \frac{1}{L_{\mathrm{n}}}}{c + d(Z(l,p)+1)}. \tag{17}$$

This expression contains two key parameters: the fast neutron deceleration length L_{n} and macroscopic atomic number of the formation Z, where L_{n} is related to the formation density and hydrogen index. These physical parameters cannot be directly measured; however, they can be derived by analyzing the detector responses. In the next section, we present a real pulsed neutron logging tool and construct a high-fidelity Monte Carlo model for analyzing these physical parameters.

2.3 Analysis of physical parameters using NGD tool

Geant4, an open-source Monte Carlo platform, was used for simulations. The tool model (Fig. 3) had a total length of 2328 mm and diameter of 188 mm and featured four neutron detectors and two gamma detectors. A boron-containing shield was positioned at the base of the neutron detectors to minimize the impact of water in the mud pipe on neutron detection. Additionally, the near-gamma detector was used for density measurement and for formation sigma and elemental measurements. A two-layer shielding structure was implemented to reduce interference from the captured gamma rays generated by the interaction of the tool with thermal neutrons. A cubic space measuring 6 m × 6 m × 6 m, with a borehole diameter of 215.9 mm, was designed to simulate the formation environment. The tool was positioned at the center of the borehole. This tool is currently under construction and will be deployed in the field upon completion.

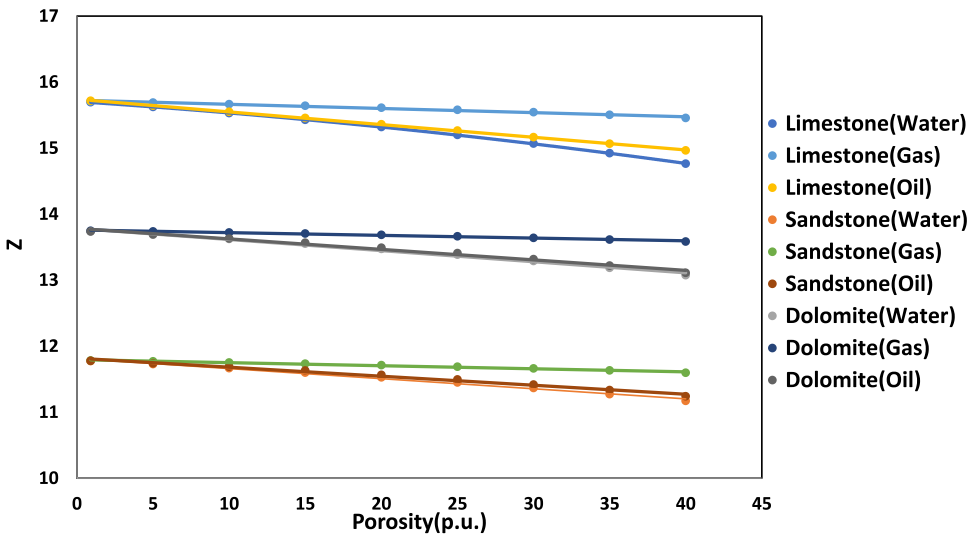

Fig. 2 (Color online) Z-results across different formations with various pore contents

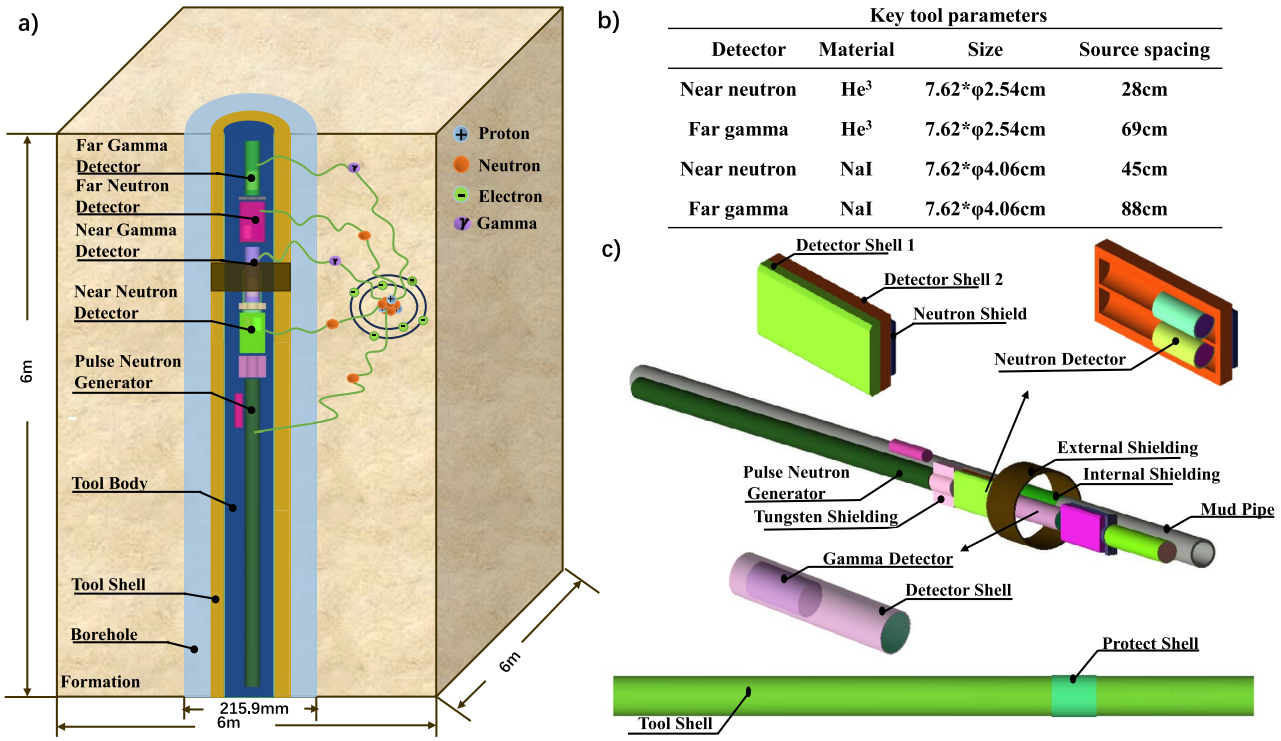

Fig. 3 (Color online) Tool model: **a** tool overview; **b** key tool parameters; **c** shielding structure

Therefore, it was selected for verifying the feasibility of the proposed method.

Extensive simulations were conducted using an NGD tool model that incorporated various formation lithologies (limestone, sandstone, and dolomite) and porosity ranges (0 p.u. to 40 p.u.). These simulations aimed to establish the relationship between the detector responses and relevant physical parameters in Eq. (17) and therefore will be used for concept validation. The specific relationships are:

(a) Hydrogen index (I_H)

The correlation between the hydrogen index and detector responses was analyzed using the simulation data. Figure 4 presents the correlation coefficients between the various detector responses and hydrogen index. These coefficients measure the strength of the linear relationship between variables, with values closer to 1 indicating a strong correlation. This analysis helps identify the optimal response for representing the hydrogen index. The features represent various detector counts: FN1 and FN2 correspond to near- and far-fast neutron counts; ENT1 and ENT2 correspond to near- and far-epithermal neutron counts; and CAP1 and CAP1 correspond to near- and far-capture gamma counts. In addition, RFN, RETN, and RCAP represent the respective ratios of fast neutrons, epithermal neutrons, and capture gamma counts. As shown in the figure, the ratio of the near-to-far epithermal neutron counts (RETN = ETN1/ETN2) exhibits the strongest correlation with the hydrogen index, making RETN the most effective indicator of hydrogen content among all detector responses.

(b) Formation density (ρ)

To accurately represent the formation density, correlation analysis was applied to evaluate the relationships between the various detector responses and density. In the figure, IN1 and IN2 represent the near- and far-inelastic gamma counts, respectively, whereas CAP1 and CAP2 represent the near- and far-capture gamma counts, respectively. RIN is the ratio of the near-to-far inelastic gamma counts and is given by RIN = IN1/IN2. In addition, RCAP is the ratio of the near-to-far capture gamma counts. RIN exhibits the strongest correlation with density, which makes it optimal for describing the density in Eq. (9) and is consistent with the principles of NGD physics [38, 39].

(c) Formation macroscopic atomic number (Z)

The macroscopic atomic number Z, which is an inherent characteristic of the formation, is strongly influenced by the lithology and pore content. By analyzing the detector counts within a specific energy window (0.07–0.35 MeV), denoted as N_{lith}, a relationship can be established to represent the

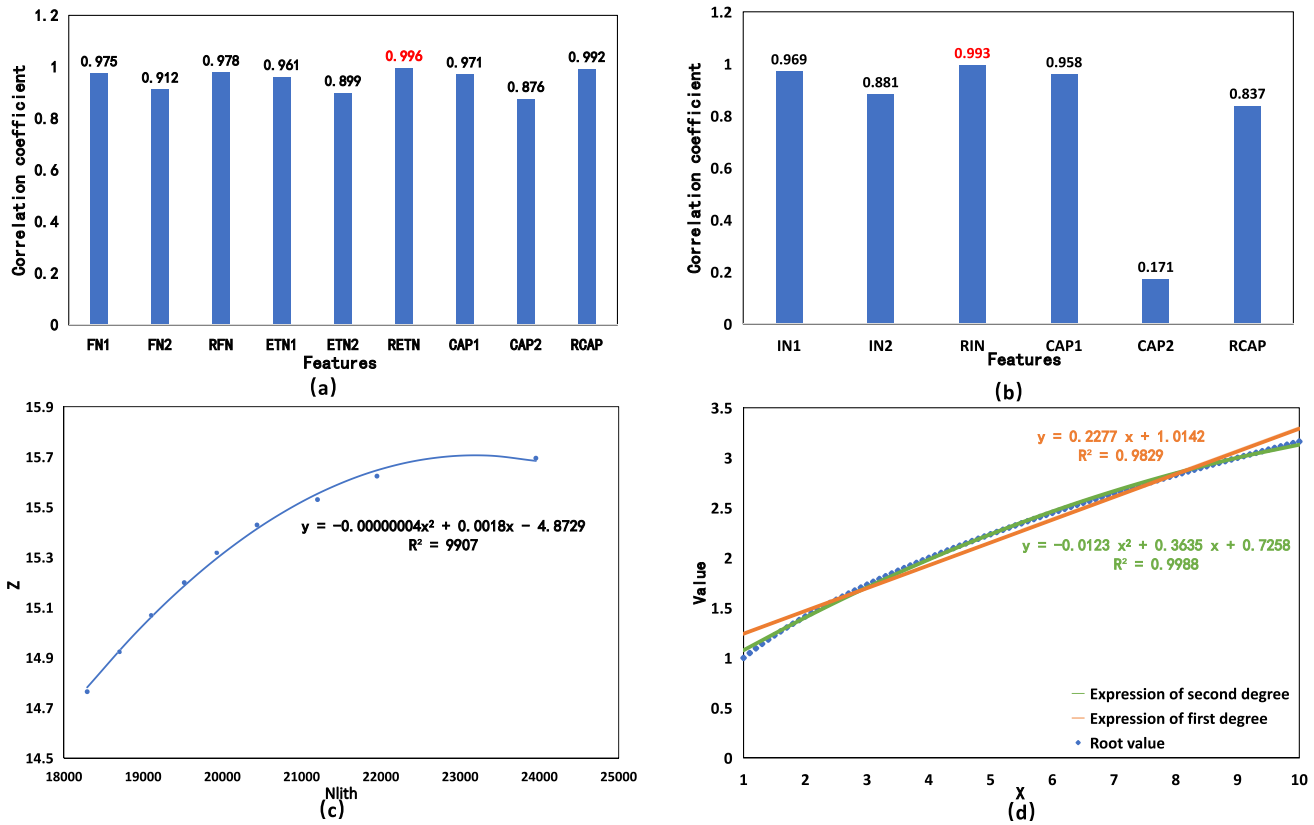

Fig. 4 (Color online) Analysis of physical parameters: **a** Hydrogen Index; **b** Density; **c** Macroscopic atomic number of limestone; **d** Polynomial fit

macroscopic atomic number. As shown in Fig. 4, this method allows the derivation of Z from the detector responses, using counts within the designated energy range to effectively characterize the macroscopic atomic number of the formation.

In summary, the density, hydrogen index, and formation macroscopic atomic number Z can be represented using RIN, RETN and N_{lith}, respectively, which can be obtained from the detector counts. Because the root term in the represented equation complicates the acquisition of the calibration coefficients, a polynomial fit approach was used to simplify the equation, as shown in the figure. After substituting the root term with a second-degree expression, Eq. (9) can be rewritten as:

$$L_{\mathrm{n}} = \frac{\tau_0}{\tau_1 \ln(\mathrm{RIN}) \times \sum_0^2 t_m (\ln(\mathrm{RETN}))^m}, \tag{18}$$

where τ_0, τ_1 and t_m (m=0,1,2) are the constants. By substituting the expression for L_{n} into Eq. (17), the density equation can be obtained as

$$\rho = \frac{\ln(\mathrm{RIN}) \times \sum_0^2 \beta_m (\ln(\mathrm{RETN}))^m}{\theta_2 (N_{\mathrm{lith}})^2 + \theta_1 N_{\mathrm{lith}} + \theta_0}, \tag{19}$$

where β_0, β_1, β_2, θ_0, θ_1, and θ_2 are the fitting parameters. Equation (19) indicates that the formation density is determined by the ratio of inelastic gamma counts RIN, ratio of epithermal neutron counts RETN, and count N_{lith}. The coefficients in the above equation using the Levenberg–Marquardt method are obtained.

3 Results and discussions

To prove the effectiveness of developing mass attenuation coefficient function, we compared two approaches for treating the mass attenuation coefficient: as a constant versus as a function of formation composition. The results demonstrated that treating it as a function significantly enhanced the calculation accuracy, thereby highlighting the effectiveness of the method. Next, we assessed the performance of the method across various environments, focusing on the formation lithology and

Table 1 Density results for different pore fluids

Porosity (p.u.)	Water (1.0 g/cm^3) Error (g/cm^3)	Gas (0.2 g/cm^3) Error (g/cm^3)	Oil (0.835 g/cm^3) Error (g/cm^3)
0.9	0.010	0.003	0.005
10	0.005	0.007	0.019
20	0.002	0.003	0.007
25	0.003	0.012	0.020
30	0.006	0.011	0.010
35	0.008	0.011	0.012
40	0.008	0.005	0.012

pore content. Finally, we considered three test cases to validate the applicability of this method to complex formations. The absolute errors were used to evaluate the calculated density results, as expressed in Eq. (19). The calculated results were considered accurate when the absolute errors were less than the threshold of 0.025 g/cm^3 [40].

$$Error = |\mathrm{DT} - \mathrm{DC}| \tag{20}$$

where Error denotes the absolute error between the calculated (DC) and true (DT) densities of the simulated formation.

3.1 Comparison of the two approaches regarding the mass attenuation coefficient

Section 2.2 emphasizes that the proposed method treats the mass attenuation coefficient as a function pertaining to the formation lithology and pore content. To evaluate the effectiveness of this method, a comparison was conducted that primarily focused on two approaches regarding the mass attenuation coefficient: treating it as a constant (denoted as h) versus treating it as a function. Based on Eq. (8) and the analysis of the relevant physical parameters in Sect. 2.3, the following equation is obtained if the mass attenuation coefficient is treated as h:

$$\rho = \frac{\ln(\mathrm{RIN}) \times \sum_0^2 \beta_m (\ln(\mathrm{RETN}))^m}{h}, \tag{21}$$

where β_0, β_1, β_2, and h are the fitting parameters. From Eq. (19), the density is determined by the ratios of the inelastic gamma counts RIN and epithermal neutron counts RETN.

Limestone with densities ranging from 2.018 g/cm^3 to 2.862 g/cm^3 was designed to compare the two approaches. Figure 5 shows the absolute density errors of both approaches. Significant differences were observed. The constant method exhibits a relatively high average absolute error of 0.048 g/cm^3, whereas the error calculated by the proposed method is reduced by approximately four times compared with that of the constant method, with an average absolute error of 0.012 g/cm^3. This demonstrates the effectiveness and

Table 2 Density results across different lithologies

Porosity (p.u.)	Limestone (g/cm^3)		Sandstone (g/cm^3)		Dolomite (g/cm^3)	
	True density	Error	True density	Error	True density	Error
0.9	2.682	0.010	2.682	0.011	2.843	0
10	2.527	0.005	2.485	0.011	2.767	0.001
20	2.358	0.002	2.320	0.011	2.674	0.001
25	2.273	0.003	2.238	0.009	2.488	0.002
30	2.188	0.006	2.155	0.007	2.395	0.001
35	2.103	0.008	2.073	0.005	2.209	0.010
40	2.018	0.008	1.990	0.009	2.116	0.003
Porosity (p.u.)	Limestone+Sandstone (g/cm^3)		Limestone+Dolomite (g/cm^3)		Sandstone+Dolomite (g/cm^3)	
	True density	Error	True density	Error	True density	Error
0.9	2.658	0.011	2.763	0.019	2.739	0.007
10	2.506	0.011	2.601	0.016	2.580	0.004
20	2.339	0.019	2.423	0.004	2.404	0.007
25	2.255	0.005	2.334	0.005	2.316	0.014
30	2.172	0.003	2.245	0.011	2.229	0.020
35	2.088	0.005	2.156	0.015	2.141	0.006
40	2.004	0.014	2.067	0.006	2.053	0.007

accuracy of the new method for measuring the formation density.

3.2 Pore content impact analysis

In NGD measurements, neutron transport is sensitive to the presence of pore content. To evaluate the effect of different pore contents on the accuracy of this method, limestone with porosities ranging from 0.9 p.u. to 40 p.u. was selected, with pores filled with water, gas, or oil. The density results for different pore contents are presented in Table 1 and Fig. 5.

Table 1 and Fig. 5 present the density calculation results for various pore contents. For the analysis, seven porosity types were selected and tested under conditions in which the pores were filled with water, oil, and gas. In limestone with water-filled pores, the Hydrogen Index I_H is equivalent to the porosity of the formation. The results indicate that I_H minimally affects density measurements. Regardless of I_H variations, the errors between the calculated and true densities were less than the threshold of 0.025 g/cm^3, demonstrating that the densities calculated using the proposed method were consistent with the true densities. In addition, this method achieved accurate measurements for high I_H formations. A comparison of the density calculations for different pore contents indicated that the absolute density errors were relatively small and remained below 0.015 g/cm^3 when the pores were filled with water or gas. However, the errors were relatively large when the pores were filled with oil. Notably, if the pores were filled with water, oil, or gas, the absolute errors were less than 0.02 g/cm^3. Thus, the method accurately determined the formation density for various porosities and pore contents.

3.3 Analysis of the effect of lithology

Because different lithologies affect neutron transport and gamma attenuation, 42 models, including limestone, sandstone, dolomite, and one-to-one mixture of any two

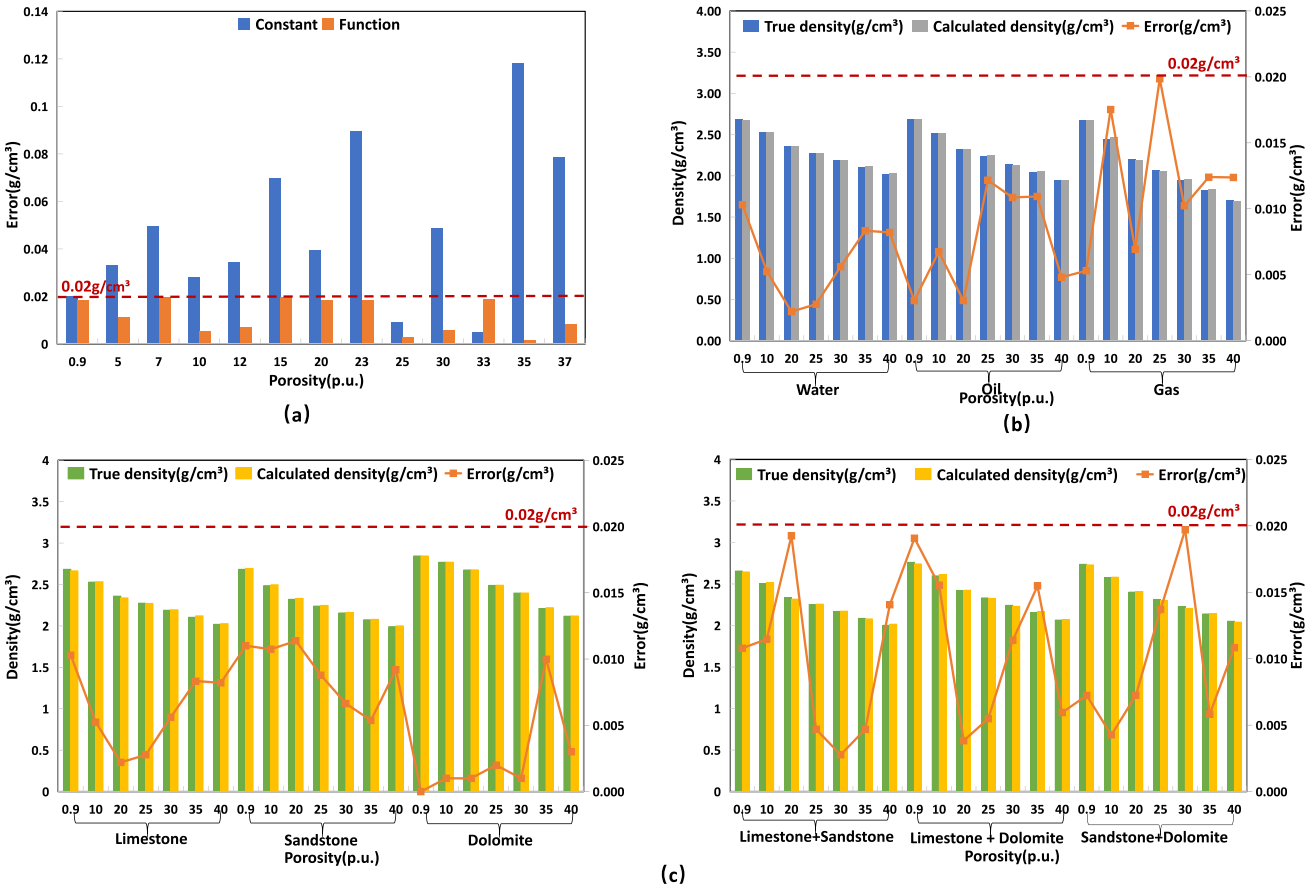

Fig. 5 (Color online) Density results: **a** Comparison of the two approaches; **b** Pore content results; **c** Lithology results

lithologies, were designed to verify the accuracy of the proposed method. All the model pores were filled with water, with porosities ranging from 0.9 p.u. to 40 p.u. The densities calculated using the proposed method were compared with the true densities used in simulated model construction, which varied between 1.93 g/cm^3 and 2.843 g/cm^3. The density results are presented in Fig. 5 and Table 2.

To verify the effect of lithology on density measurements, the present study focused on a single lithology (clean formations) and mixed lithology comprising sandstone, limestone, and dolomite. Table 2 shows slight differences in the density results across various lithologies, and the average absolute error in the mixed lithology is slightly larger than that in the single lithology, possibly owing to the complexity of the composition of the formation. Regardless of whether it was a single or mixed lithology, the calculated densities were consistent with the true densities, and the absolute density errors were less than 0.02 g/cm^3. Overall, the average absolute error in the test database was 0.009 g/cm^3, confirming the accuracy of the proposed method for different lithologies.

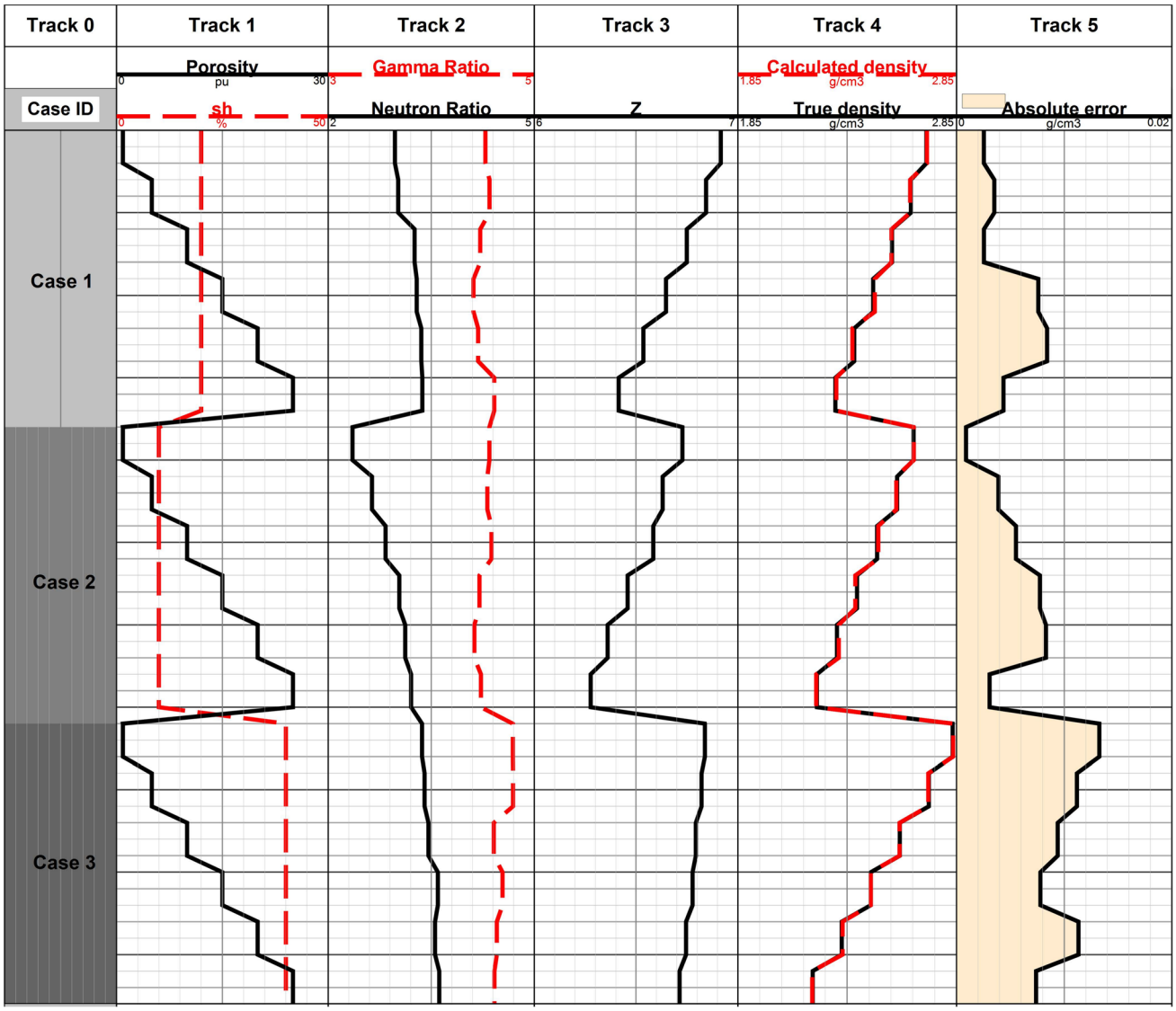

Fig. 6 (Color online) Results and comparisons. Track 0: Case 1, Case 2 , and Case 3. Track 1: Case parameters, including porosity and mud content in the formation. Track 2: Detector counts, including the inelastic gamma count ratio LNRIN, and the epithermal neutron count ratio LNRETN. Track 3: Macroscopic atomic number of the formation. Track 4: Comparison of the true and calculated densities. Track 5: Absolute error

3.4 Multi-parameter impact analysis

The above results quantitatively analyze the impact of lithology and pore content on the accuracy of the density measurement. To further evaluate the proposed method, three cases (Cases 1, 2, and 3) were designed, representing three lithologies (limestone, sandstone, and dolomite) and three pore contents (water, oil, and gas), while considering the mud components (such as chlorite). Specifically, Case 1 simulates water-filled limestone with 20% chlorite; Case 2 simulates oil-filled sandstone with 10% chlorite; and Case 3 simulates dolomite-containing gas with a relatively high chlorite content of 40%. In all these cases, the borehole size was 8.5 in, with a porosity range set from 0 p.u. to 25 p.u., and formation densities between 2.211 g/cm^{3}and 2.712 g/cm^3. The results are shown in Fig. 6.

The inelastic gamma and epithermal neutron ratios varied across formations with different lithologies and pore contents, highlighting the effect of formation composition on neutron transport and gamma attenuation. In particular, cases 1 and 2 exhibited smaller measurement errors, demonstrating higher accuracy. In contrast, Case 3 exhibited relatively higher measurement errors, possibly because of its more complex formation composition, characterized by elevated mud content and gas-filled pores. Nevertheless, the absolute density errors in all three cases remained below 0.02 g/cm^3, demonstrating the accuracy and reliability of the proposed method for measuring the formation density.

3.5 Tool calibration

Owing to the scarcity of commercial tools worldwide, the experimental validation of the NGD tool is briefly discussed in this work using Schlumberger's work, which introduces an NGD calibration process [40]. The step-by-step process is summarized as follows:

Step 1: Preparation for calibration. A large water-filled calibration tank was used. Access to the aluminum sleeve and the ability to control the fluid in the mud channel (air or water) were ensured.

Step 2: Performing multiple distinct measurements. Measurements across a wide dynamic range were performed under designated configurations: with aluminum sleeve and water in the mud channel, with aluminum sleeve and air in the mud channel, without aluminum sleeve and water in the mud channel, and without aluminum sleeve and air in the mud channel.

Step 3: Fitting a linear model and evaluating the fit The best linear fit was applied to the calibration data points. χ^2 was calculated to assess the goodness of the fit.

Step 4: Repeatability Check. The calibration process was repeated multiple times without altering the tool or setup. Consistency in the calibration gain was ascertained, particularly for critical parameters.

Step 5: Analyze and Compare. Calibration gains across repeated runs were compared to ensure the reliability of the calibration process.

The multiple configurations employed in this approach effectively established a set of measurement boundary conditions. This design enhanced the dynamic range of the detector count rates and improved the calibration accuracy. The calibration process considers the unique characteristics of NGD tools and can be extended to future NGD tools. Further research, along with calibration and field data acquisition, is planned to validate the practical utility of the proposed method after the development of a new version of the NGD tool.

4 Conclusion

(1) A new mass attenuation coefficient function of formation lithology and pore content was introduced. Based on the study of the neutron-induced gamma attenuation process, the mass attenuation coefficient was found to vary according to the formation parameters. Therefore, it may be considered as a function to better evaluate the effects of environmental variables on gamma attenuation.

(2) A new density measurement method was developed by employing the concept of mass attenuation coefficient function that evaluated the effects of formation composition on gamma attenuation. The method employed inelastic gamma rays for density measurement while incorporating epithermal neutrons to correct for neutron transport, for example, the influence of fast neutrons on the spatial distribution and intensity of inelastic gamma rays. The proposed method integrated information from both neutrons and gamma rays to accurately evaluate interaction mechanisms between radiation and formation and obtain precise density measurements.

(3) An elaborate NGD tool model was developed and employed to verify the performance of the proposed method. The proposed method was evaluated using 63 sets of simulated models of varying lithologies and pore contents. The results showed that the absolute errors of the densities calculated using the proposed method were below 0.02 g/cm^3 for all the cases. Specifically, the same level of accuracy was achieved in mixed cases, proving its effectiveness. Therefore, this

can provide theoretical support for designing new NGD tools.

The proposed method faces challenges under extreme environmental conditions and tool calibration. For example, under logging-while-drilling downhole conditions, such as high temperature (150 °C) and high pressure (2000 psi), the performance of the detectors and electronics of the tool may be affected. In addition, the physical properties of borehole fluids may change, thus affecting measurement accuracy. Furthermore, this method relies significantly on calibration coefficients, which requires high-level calibration standards in tool-specific environments. Further research is required to improve the applicability of the proposed method.

Author Contributions All authors contributed to the study conception and design. Material preparation, data collection and analysis were performed by Chen Junyan and Zhang Qiong. The first draft of the manuscript was written by Chen Junyan, and all authors commented on previous versions of the manuscript. All authors read and approved the final manuscript.

Data Availability The data that support the findings of this study are openly available in Science Data Bank at https://cstr.cn/31253.11.sciencedb.j00186.00823 and https://doi.org/10.57760/sciencedb.j00186.00823.

Declarations

Conflict of interest The authors declare that they have no Conflict of interest.

References

1. R. Spross, T. Burnett, J. Freeman et al., Formation density measurement while drilling. at the SPWLA 34th Annual Logging Symposium. (Alberta, 1993). https://doi.org/10.30632/SPWLA-1993-PP
2. Q. Zhang, Y. Wang, Formation density and photoelectric index calculation using an ultra-slim density tool. Geo. Sci. Eng. **237**, 212817 (2024). https://doi.org/10.1016/J.GEOEN.2024.212817
3. Y.L. Li, Q. Zhang, A novel constraint-based method for density measurement in cased hole. Geo. Sci. Eng. **228**, 211954 (2023). https://doi.org/10.1016/J.GEOEN.2023.211954
4. X.Y. Wang, Q. Zhang, High-efficiency monte carlo simulation based on CADIS method for Gamma density measurement. Ann. Nucl. Energy **185**, 109710 (2023). https://doi.org/10.1016/j.anucene.2023.109710
5. Q. Zhang, Y.L. Li, Y. Jin et al., A new gamma density measurement method for cased-hole formation evaluation. Appl. Radiat. Isot. **184**, 110178 (2022). https://doi.org/10.1016/j.apradiso.2022.110178
6. H.W. Yu, Y.X. Zhang, X.H. Chen et al., Numerical simulation and method study of X-ray litho-density logging. Nucl. Sci. Tech. **31**(12), 124 (2020). https://doi.org/10.1007/s41365-020-00826-2
7. Y. Ge, J. Liang, Q. Zhang et al., A comparison study of GEANT4 and MCNP6 on neutron-induced gamma simulation. Appl. Radiat. Isot. **190**, 110514 (2022). https://doi.org/10.1016/j.apradiso.2022.110514
8. T. Gjerdingen, J. Hilton, N. Bounoua et al., Sourceless neutron-density porosity determination: fit-for-purpose formation evaluation with significant HS &E benefits. at SPE annual technical conferences and exhibitions. (Texas, 2012). https://doi.org/10.2118/159522-MS
9. G. Schmid, R. Pemper, D. Dolliver et al., A diffusion-corrected sigma algorithm for a four-detector pulsed-neutron logging tool. In: SPE Annual Technical Conference and Exhibition. (Texas, 2018). https://doi.org/10.2118/191738-MS
10. J. Liu, S. Liu, S. Zhang et al., A method for evaluating gas saturation with pulsed neutron logging in cased holes. J. Nat. Gas. Sci. Eng. **59**, 354–362 (2018). https://doi.org/10.1016/j.jngse.2018.09.018
11. F. Zhang, Q.Y. Zhang, J.T. Liu et al., A method to describe inelastic gamma field distribution in neutron gamma density logging. Appl. Radiat. Isot. **129**, 189–195 (2017). https://doi.org/10.1016/j.apradiso.2017.08.024
12. H. Wang, A.Z. Yue, X.L. Zhang et al., Bulk density response and experimental study of pulsed neutron-gamma density logging. Front. Earth. Sci. **10** (2022). https://doi.org/10.3389/FEART.2022.803775
13. Q.Y. Zhang, R. Deng, S.Q. Zhang et al., An alternative method for sourceless density measurement with boron sleeve gamma detectors. Appl. Radiat. Isot. **174**, 109785 (2021). https://doi.org/10.1016/j.apradiso.2021.109785
14. M. Luycx, T.V. Carlos, Rapid forward modeling of logging-while-drilling neutron-gamma density measurements. Geophysics **83**(6), D231–D246 (2018). https://doi.org/10.1190/geo2018-0142.1
15. L. Zhang, H.W. Yu, W.B. Jia et al., Study on the influence of formation factors on spatial distribution of D-D induced γ-ray source. Nucl. Tech. (in Chinese) **42**(1), 010501 (2019). https://doi.org/10.11889/j.0253-3219.2019.hjs.42.010501
16. R.C. Odom, R.W. Streeter, G.P. Hogan et al., A new 1.625" diameter pulsed neutron capture and inelastic/capture spectral combination system provides answers in complex reservoirs. In: SPWLA 35th annual logging symposium. (Oklahoma 1994). https://doi.org/10.30632/SPWLA-1994-O
17. M.P. Archer, R.C. Odom, R.D. Wilson et al., Pulsed neutron density measurements: modeling the depth of investigation and cased-hole wellbore uncertainties. In: SPWLA 40th annual logging symposium. (Norway, 1999). https://doi.org/10.30632/SPWLA-1999-JJ
18. L. Jacobson, D. Durbin, S. Reed, An improved formation density measurement using PNC tools. In: SPE annual technical conference and exhibition. (Texas, 2004). https://doi.org/10.2118/90708-MS
19. Q.Y. Zhang, F. Zhang, J.T. Liu et al., A method of determining formation density based on fast-neutron gamma coupled field theory. Petrophysics. **58**(04), 411–425 (2017). https://doi.org/10.30632/SPWLA-2017-v58n4a6
20. M. Luycx, T.V. Carlos, Physics, applications, and limitations of borehole neutron-gamma density measurements. Geophysics **84**(1), D39–D56 (2018). https://doi.org/10.1190/geo2018-0088.1
21. H. Wang, W.S. Wu, R.G. Wang et al., Neutron transport correction and density calculation in the neutron-gamma density logging. Appl. Radiat. Isot. **150**, 110–119 (2019). https://doi.org/10.1016/j.apradiso.2019.05.023
22. Q. Zhang, Source less density measurement using an adaptive neutron-induced gamma correction method. Nucl. Sci. Tech. **34**, 125 (2023). https://doi.org/10.1007/s41365-023-01274-4
23. D.V. Ellis, J.M. Singer, Well Logging for Earth Scientists (Springer, 2007)
24. X. Fu, W. Wu, H. Wang et al., A new neutron-gamma porosity measurement method for pulsed neutron logging tools.

Geophysics **88**(4), 1–55 (2023). https://doi.org/10.1190/geo2022-0471.1
25. Q. Zhang, F. Zhang, C. Yuan et al., A comparative study on the neutron-gamma density and gamma-gamma density logging. J. Petrol. Sci. Eng. **176**, 792–799 (2019). https://doi.org/10.1016/j.petrol.2019.02.007
26. S. Mahiout, A. Belowi, A. Alqunais et al., Impact of improved neutron-gamma density measurement while drilling in formation evaluation - a case study. In: SPE annual technical conference and exhibition. (UAE, 2016). https://doi.org/10.2118/181279-MS
27. W. Tang, J.G. Liang, Y. Ge et al., A method for neutron-induced gamma spectra decomposition analysis based on Geant4 simulation. Nucl. Sci. Tech. **33**, 12 (2022). https://doi.org/10.1007/s41365-022-01144-5
28. Q. Zhang, L.L. Lin, A fast forward computational method for nuclear measurement using volumetric detection constraints. Nucl. Sci. Tech. **35**, 31 (2024). https://doi.org/10.1007/s41365-024-01393-6
29. W.C. Li, Q.X. Zhang, H.X. Wu et al., A gamma ray sourceless efficiency calibration method based on the Boolean operation of the ray deposition process. Appl. Radiat. Isot. **193**, 110620 (2023). https://doi.org/10.1016/j.apradiso.2022.110620
30. W. Wu, N. Wei, L. Li, Quantitative analysis of neutron capture gamma-ray energy spectra using direct demodulation. Pet. Geosci. **79**(2), D91–D98 (2014). https://doi.org/10.1190/geo2013-0296.1
31. Q.Y. Zhang, F. Zhang, C. Yuan et al., Application analysis on the different neutron gamma density (NGD) logging methods. Appl. Radiat. Isot. **172**, 109672 (2021). https://doi.org/10.1016/j.apradiso.2021.109672
32. L. Zhang, H.W. Yu, W.B. Jia et al., Improved formation density measurement using controllable D-D neutron source and its lithological correction for porosity prediction. Nucl. Sci. Tech. **33**, 3 (2022). https://doi.org/10.1007/s41365-022-00988-1
33. Y.L. Fu, Numerical simulation of pulse neutron density logging method and tool design. Northeast Petroleum University (2019). https://doi.org/10.26995/d.cnki.gdqsc.2019.000451
34. H. Wang, W.S. Wu, H.W. Wang et al., Formation density affects and corrections in pulsed neutron porosity logging. Nucl. Tech. (in Chinese) **41**(08), 65–71 (2018). https://doi.org/10.11889/j.0253-3219.2018.hjs.41.080406
35. S.F. Ajzenberg, Nuclear spectroscopy (Academic Press, 1960)
36. K. Siegbahn, α, β, γ-ray spectroscopy (North-Holland Publishing Company, 1965)
37. H.W. Yu, Z. Wang, Z.B. Xue et al., Corrections of fast neutron inelastic scattering effects on D-T neutron porosity logging. Appl. Radiat. Isot. **190**, 110486 (2022). https://doi.org/10.1016/J.APRADISO.2022.110486
38. H. Wang, W.S. Wu, T.Z. Tang et al., A new method for calculating bulk density in pulsed neutron-gamma density logging. Geophysics **85**, 06 (2018). https://doi.org/10.1190/geo2018-0821.1
39. D. Dong, W.S. Wu, W.Z. Yue et al., Improving the pulsed neutron-gamma density method with machine learning regression algorithms. J. Petrol. Sci. Eng. **218**, 110962 (2022). https://doi.org/10.1016/j.petrol.2022.110962
40. M.L. Mauborgne, R. Rodriguez, F. Allioli et al., Enhancing accuracy and range of sourceless density. In: SPWLA 65th annual logging symposium. (Brazil, 2024). https://doi.org/10.30632/SPWLA-2024-0108